Supporting information

Crystal Facets Evolution of Spinel Co_3O_4 Nanosheets in Acidic Oxygen Evolution Catalysis

Ziyang Sheng,[a] Sihong Wang,[a] Qu Jiang,[a] Yuanman Ni,[a] Chaoran Zhang,[a] Ashfaq Ahmad,[a] and Fang Song,[a*]

[a]State Key Laboratory of Metal Matrix Composites, School of Materials Science and Engineering, Shanghai Jiao Tong University, Shanghai 200240, China

[*] Corresponding authors: songfang@sjtu.edu.cn

EXPERIMENTAL SECTION

General.

All chemicals were directly used as they were received from manufacturers. Double-sided hydrophilic carbon paper (TGP-H-060) was purchased from TORAY. Cobalt(II) nitrate hexahydrate (99%) was obtained from Aladdin. 5 wt.% Nafion solution was obtained from Alfa Aesar. Sulfuric acid (95.0-98.0%), Hydrochloric acid, acetone, and anhydrous ethanol were purchased from Sinopharm Group. Millipore-Q water (18.2 MΩ) was used for all the measurements and synthesis.

Characterization

The crystallographic information of Co_3O_4 on carbon paper was collected by Mini Flex 600 with Cu Kα irradiation (λ = 1.5406 Å) at 40 kV and 40 mA in the 2θ range of 30 to 80° with a scanning rate of 10°/min. TESCAN MIRA3 field emission scanning electron microscopy (FE-SEM) and accompanying energy dispersive spectroscopy (EDS) was applied to confirm the morphology and elements of the products. Transmission electron microscopy (TEM) and high-resolution Transmission electron microscopy (HRTEM) was collected by Talos F200X G2 FETEM under an acceleration voltage of 200 kV. X-ray photoelectron spectroscopy (XPS) analysis was obtained by AXIS UltraDLD and all spectra were corrected using C 1s line at 284.6 eV. Inductively coupled plasma-mass spectrometry(ICP-MS) was used to test the metal element contained in the electrolyte by i CAP Q.

Synthesis of Co_3O4 nanosheets.

Firstly, Hydrophilic carbon paper was cut into small pieces with designated sizes. They were dipped into an aqueous solution mixed with 20 mL acetone and 20 mL 3 M HCl for 10 min under ultrasonication conditions. The carbon papers were then washed with 20 mL deionized water and 20 mL anhydrous ethanol by ultrasonication for 10 min. Following this, the carbon papers were taken out and dried at 60 ℃ for use.

The cleaned carbon papers were held with a glassy carbon electrode clamp

at one end and were used as working electrodes. A three-electrode system was constructed with 50 mL 0.1M $Co(NO_3)_2$ aqueous solution as the electrolyte, 10*10* 0.1mm platinum electrode as the counter electrode, and saturated silver chloride electrode as the reference electrode. Gamry electrochemical workstation was used for electrodeposition at -2 mA constant current for 1000s. After the electrodeposition was completed, the carbon paper was soaked and rinsed in deionized water several times and dried in a 60℃ vacuum for 12 h. Finally, the blue-green carbon paper loaded with α-cobalt hydroxide was obtained.[1,2]

The dried α-$Co(OH)_2$/CP was placed in the ceramic ark and heat-treated by a quartz tube furnace. In order to retain the morphology of cobalt hydroxide, the heating rate of 1 ℃/min was adopted to 300 ℃, and the temperature was cooled to a normal temperature at 1 ℃/min after holding for 2 h, and then the array of cobalt tetroxide nanosheets supported on carbon paper (Co_3O_4/CP) was obtained.[3]

In order to reduce the physical peeling of the nanosheets in the agitated electrolyte, 15μL Nafion dispersion (anhydrous ethanol, deionized water, and 5%Nafion polymer volume ratio 8:1.5:0.5) was added to both sides of the carbon paper and dried at 60℃ for 30 min before the electrochemical test.

Math methods.

Decoupling of redox peaks is achieved through Origin2023's Peak Deconvolution feature. After deducting the background current, the initial predicted positions of the three Gaussian peaks were set manually, and then the peak areas and peak positions of the three reduction peaks were obtained by automatically fitting.

Electrochemical measurements.

All electrochemical characterizations were investigated on Gamry Reference600+ potentiostat in a three-electrode configuration cell using Co_3O_4/CP with a precisely controlled active area of 1 cm^2 as working electrode,

platinum plate (1×1 cm^2) as the counter electrode and calibrated saturated Silver/chloride silver (Ag/AgCl) as the reference electrode at room temperature. The electrolyte was mixed with 0.5 M H_2SO_4 and 0.5 M Na_2SO_4 solution to ensure the cation concentration is 1 M. The potentials were referenced to the RHE ($E_{RHE} = E_{Ag/AgCl} + 0.196\ V + 0.0592*pH\ V$). iR compensation was realized by the CI function of the potentiostat. The voltammetry cycle curve was obtained at a sweep speed of 5 mV s^{-1}. The analysis of the reduction peak pattern is based on the reverse sweep curve of CV (See more detail in supplementary methods). Electrochemical surface area (ECSA) was obtained by linear fitting of the average charge-discharge current of the CV curve at sweep speeds of 10, 60, 110, and 160 mV s^{-1} near the open-circuit potential. Electrochemical impedance spectroscopy is obtained at a fixed potential with an amplitude of 10 mV at a frequency from 0.1 to 20kHz.

Computational methods.

According to the XRD and TEM analysis, Co_3O_4 ($Fd\bar{3}m$ space group) was used as the computational model. To model the dissolution process under OER conditions, oxygen-path and metal-path containing OOH intermediates were considered in the calculations. In this work, Co^{2+} was considered as the dissolved product of Co_3O_4 in acidic conditions and the energy of Co^{2+} was corrected to an electrode potential of −1.7 V versus RHE based on the standard redox potential ($Co^{2+} + 2e^- \leftrightarrow Co(s)$, $U' = -0.28\ V$). All calculations were carried out within the context of periodic density functional theory (DFT), as implemented in the Vienna ab initio simulation package (VASP), version 5.4.4. The core electrons were described by using the projector augmented plane-wave (PAW) pseudopotential. For each facet, we adopted a Gamma-point centered k-point mesh. The cut-off energy of the plane wave was set to 450 eV and the energy convergence criterion for the self-consistent-field (SCF) cycles was set to 10^{-6} eV per cell. The electrode potentials were corrected to the experimental current density of 10 mA cm^{-2}_{geo} at 1.623 V versus RHE for Co_3O_4 in the calculation of the reaction energies.

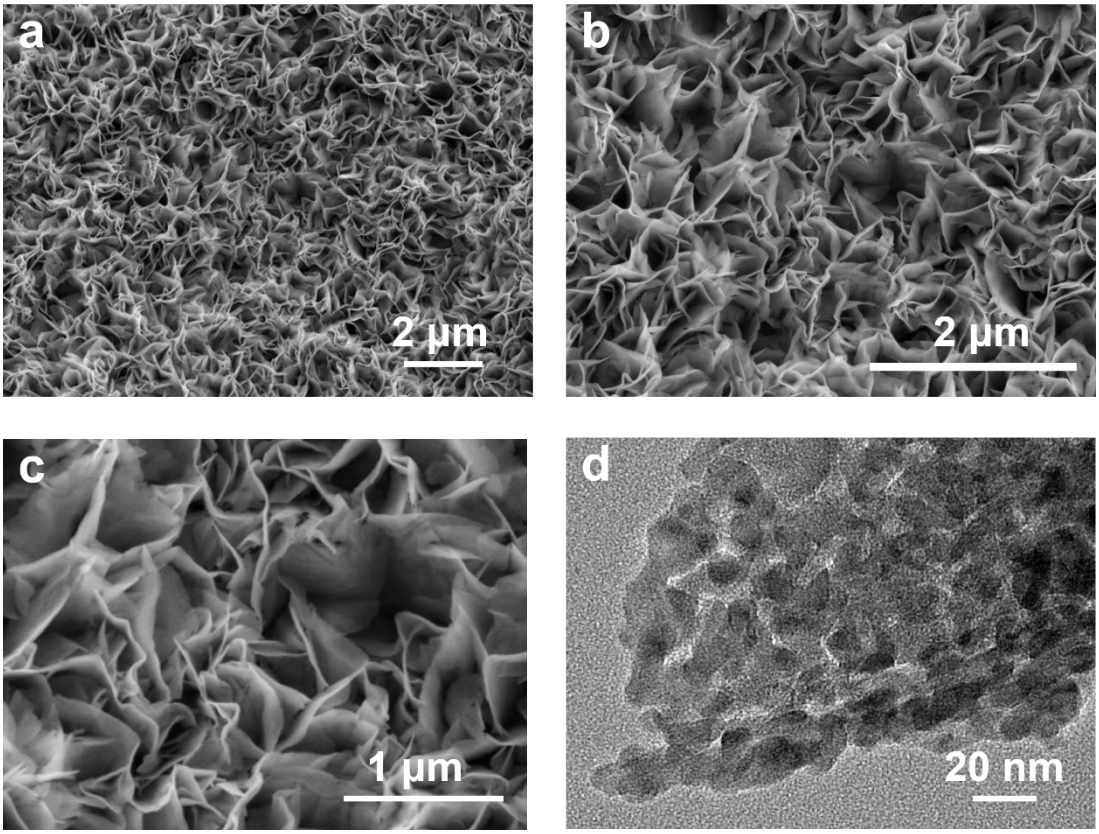

Figure S1. Microstructures of Co_3O_4 nanosheets, **a-c)** SEM image, **d)** TEM image.

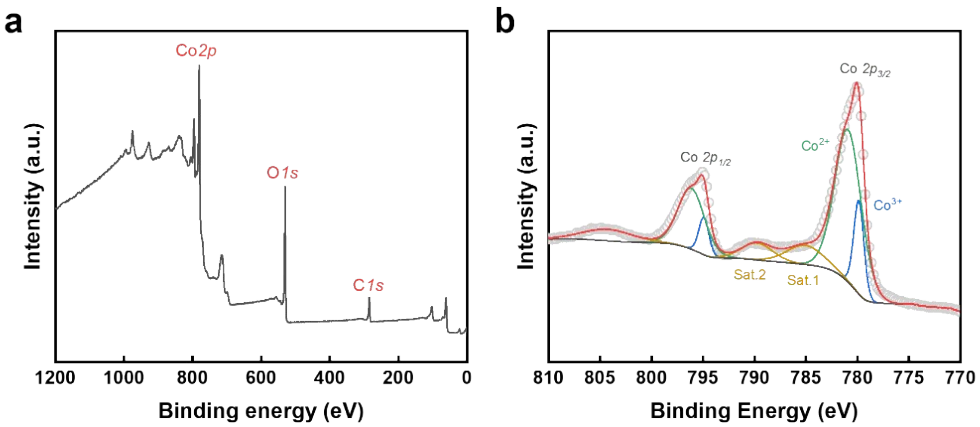

Figure S2. XPS of Co_3O_4 before OER reaction. **a)** XPS survey spectra. **b)** High-resolution spectra of Co_{2p}. The Co_{2p} spectra were fitted by considering two spin-orbit doublets characteristic of Co^{2+}, $Co^{3+,}$ and shakeup satellites.

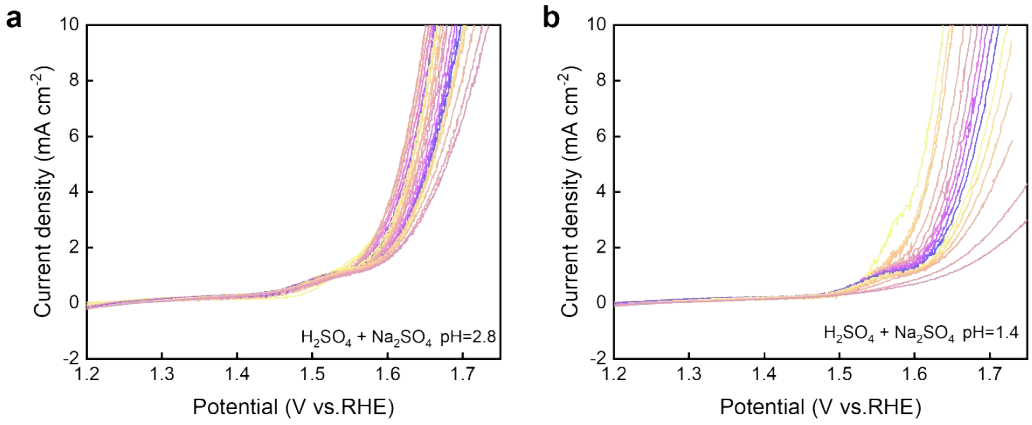

Figure S3. Evolution of LSV scans of Co_3O_4 nanosheets at different times in electrolytes of **a)** pH=2.8 and **b)** pH=1.4. There is a one-hour interval between each curve. Co_3O_4 had a more stable oxidation peak (~1.52 V vs. RHE) in the electrolyte of pH=2.8 over that of pH=1.4.

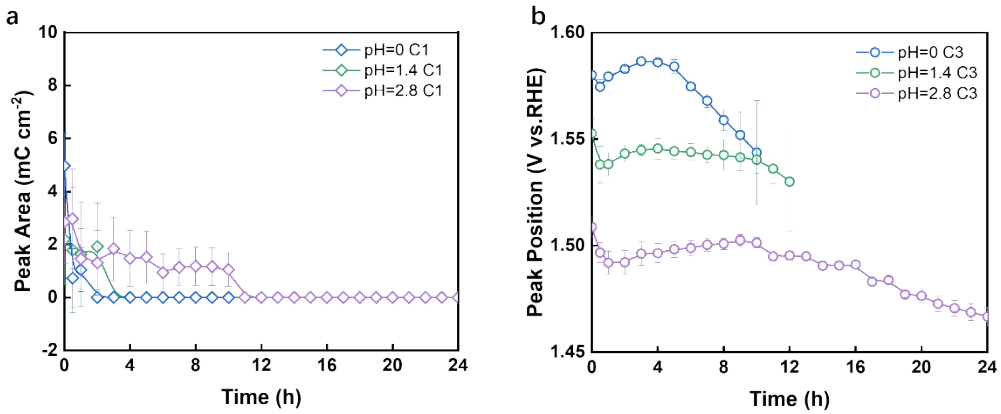

Figure S4. Peak areas of **a)** C1 and **b)** C3 plotting against the electrolysis time at pH= 0, 1.4, and 2.8. The fitting parameters are listed in Table S3-S5.

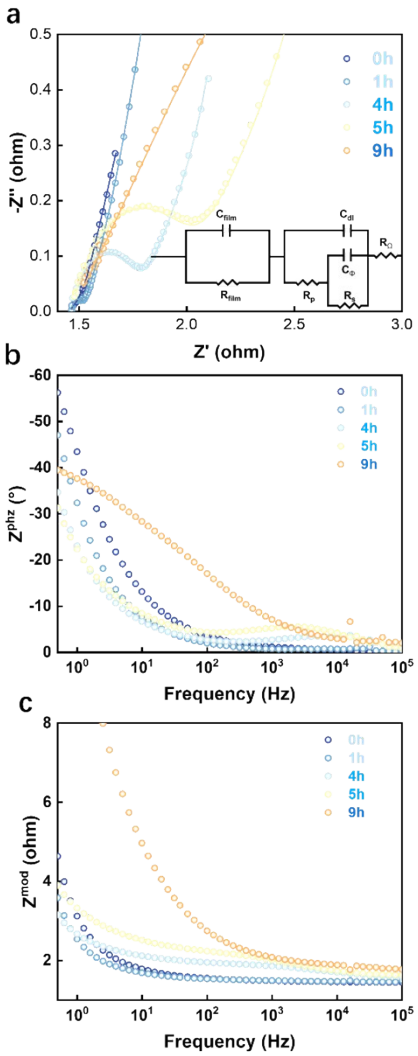

Figure S5. EIS of Co_3O_4 catalysts at different times. **a)** Nyquist plots. **b, c)** Bode plots. The inset in a) shows the circuit model used for fitting. We used a "thick-film interfacial adsorption model" to quantify the adsorption/desorption behavior at the interface of thick-film catalysts.[4,5] The fitting parameters are listed inTable S4. R_Ω, C_{dl}, $R_{film,}$ and C_{film} correspond to the solution resistance, double-layer capacitance, thick-film resistance, and capacitance, respectively. R_s is a charge transfer resistance controlled by the adsorption/desorption process of the intermediate. R_p refers to a resistance related to charging transfer. C_Φ is the charge relaxation of the adsorbed intermediates.

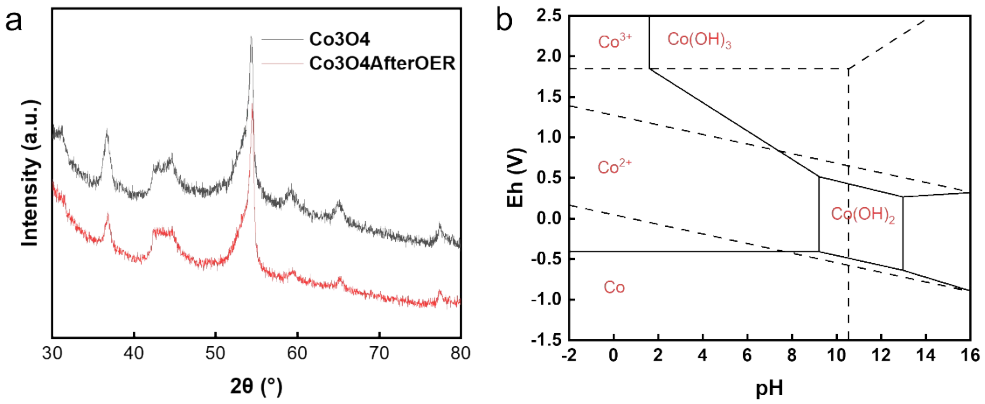

Figure S6. a) XRD patterns of Co_3O_4 nanosheets on carbon paper after electrolysis in 0h and 9h. Co_3O_4 maintains the original phase structure. No new phase is generated. **b)** Pourbaix diagram of cobalt [6].

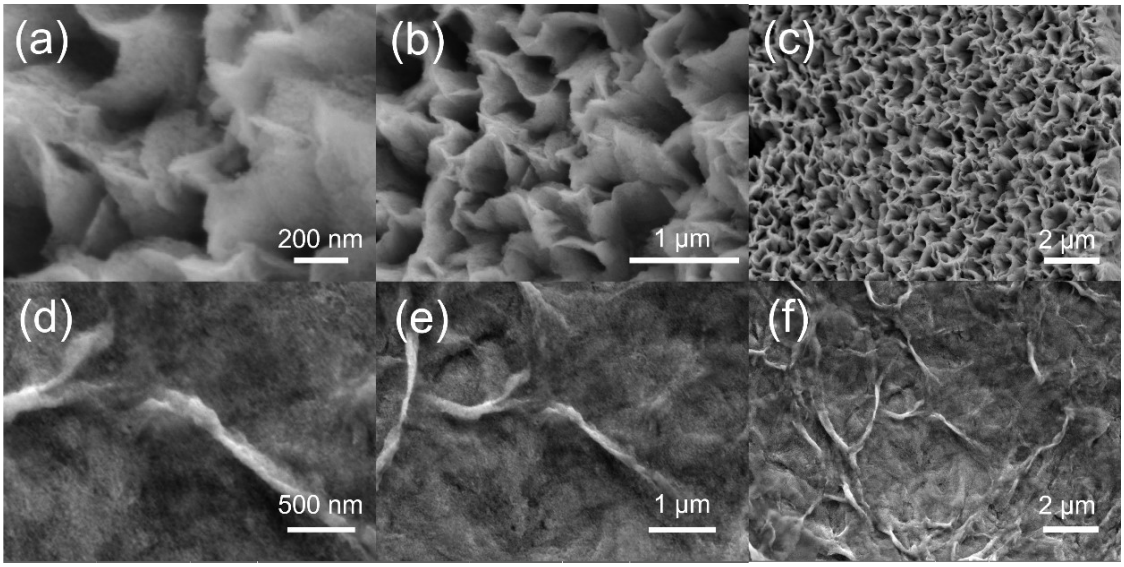

Figure S7. SEM image of Co_3O_4 after acidic OER of 9h. **a-c)** Weakly dissolved region. **d-f)** Intensely dissolved region.

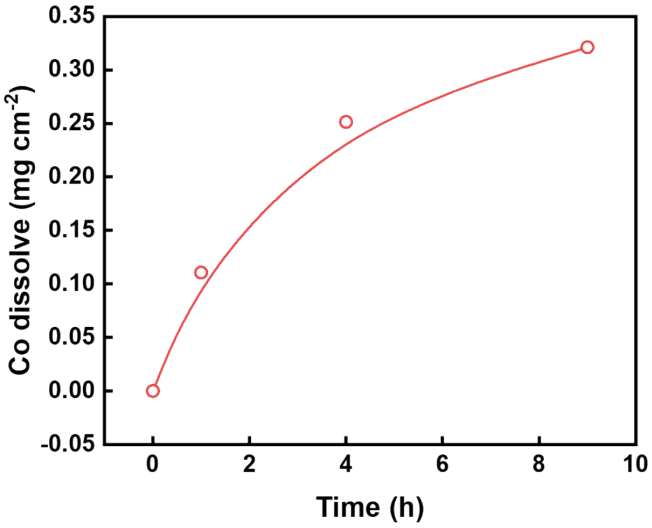

Figure S8. Mass of Co in the electrolyte (pH=0) at 0h, 1h, 4h, and 9h. The mass was measured by ICP-MS.

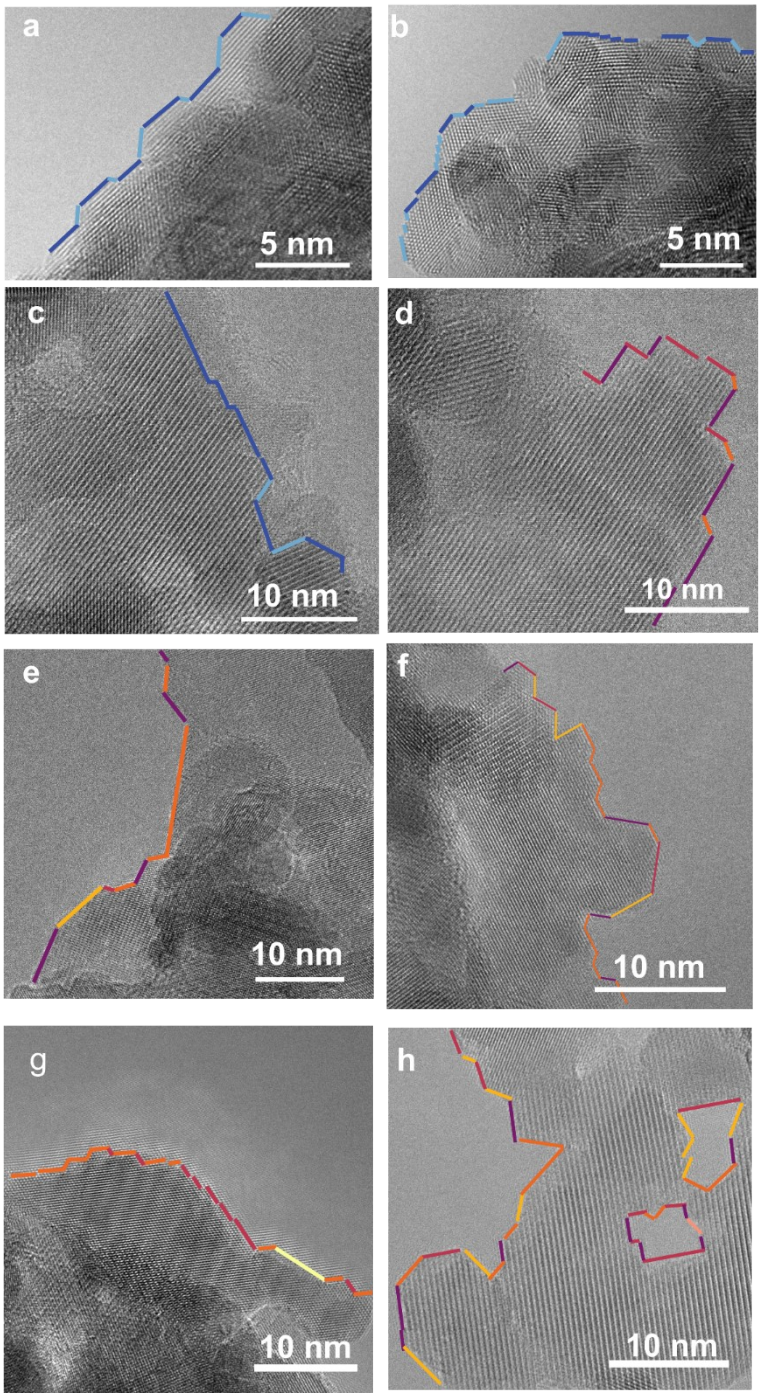

Figure S9. HRTEM images with labeled crystal facets of Co_3O_4 nanosheets at different times. **a, b)** 0h. **c, d)** 1h. **e, f)** 4h. **g, h)** 9h.

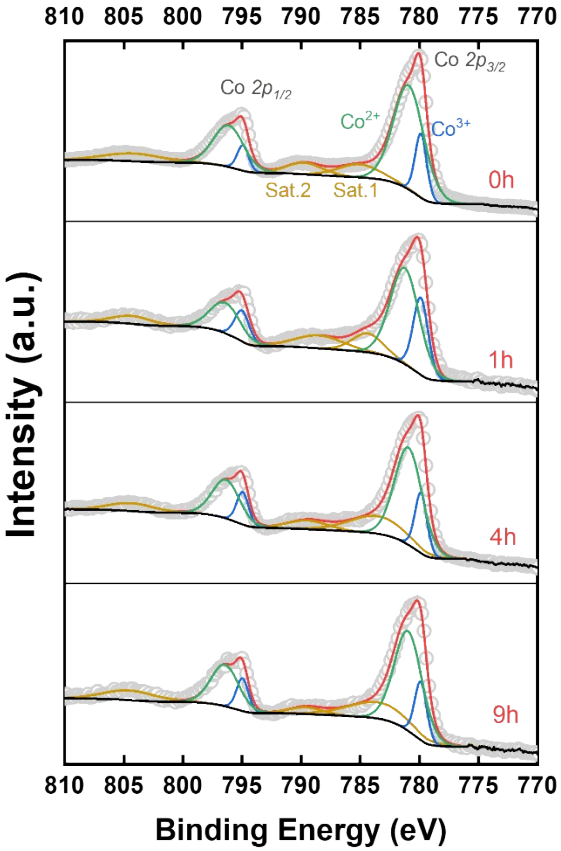

Figure S10. Co_{2p} XPS spectra of Co_3O_4 nanosheets after electrolysis for 1h 4h and 9h. The fitting parameters are listed in Table S1.

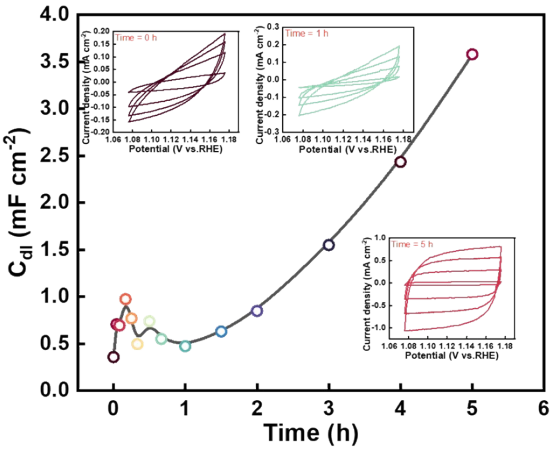

Figure S11. Evolution of electrochemical active surface area (ECSA) of Co_3O_4 nanosheets during the deactivation in pH=0 electrolyte. The insets show the ECSA curves at 0h, 1h, and 5h.

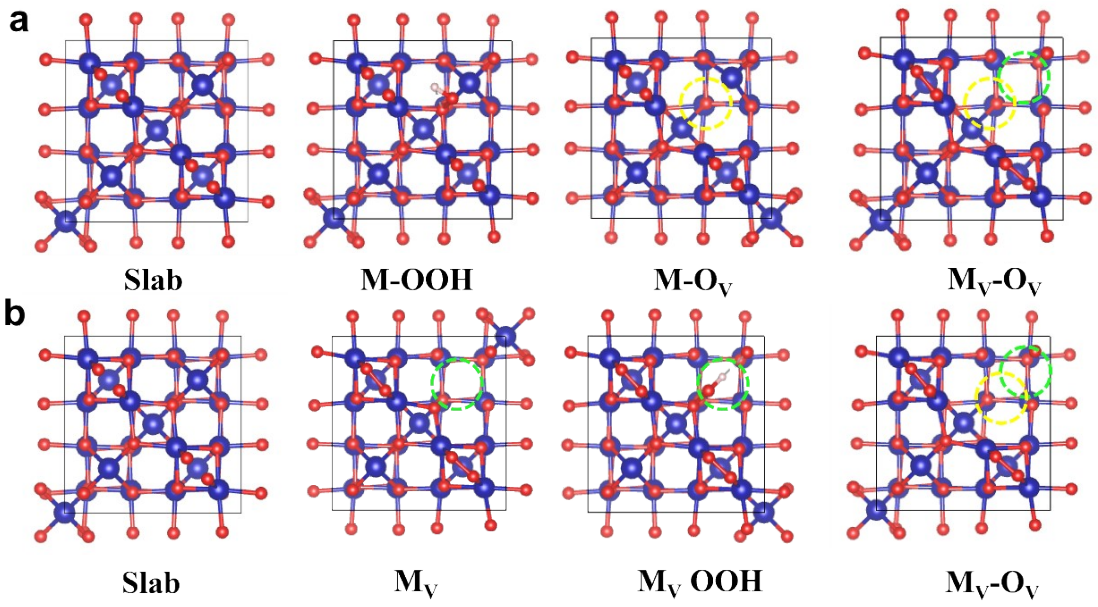

Figure S12. Top view of the model of Co_3O_4 {100} crystal plane in the deactivation process. **a)** O-path. **b)** M-path of Co3. The red sphere is an oxygen atom, the blue sphere is a cobalt atom, and the white sphere is a hydrogen atom. The yellow dashed circles correspond to oxygen vacancies and the green corresponds to metal vacancies.

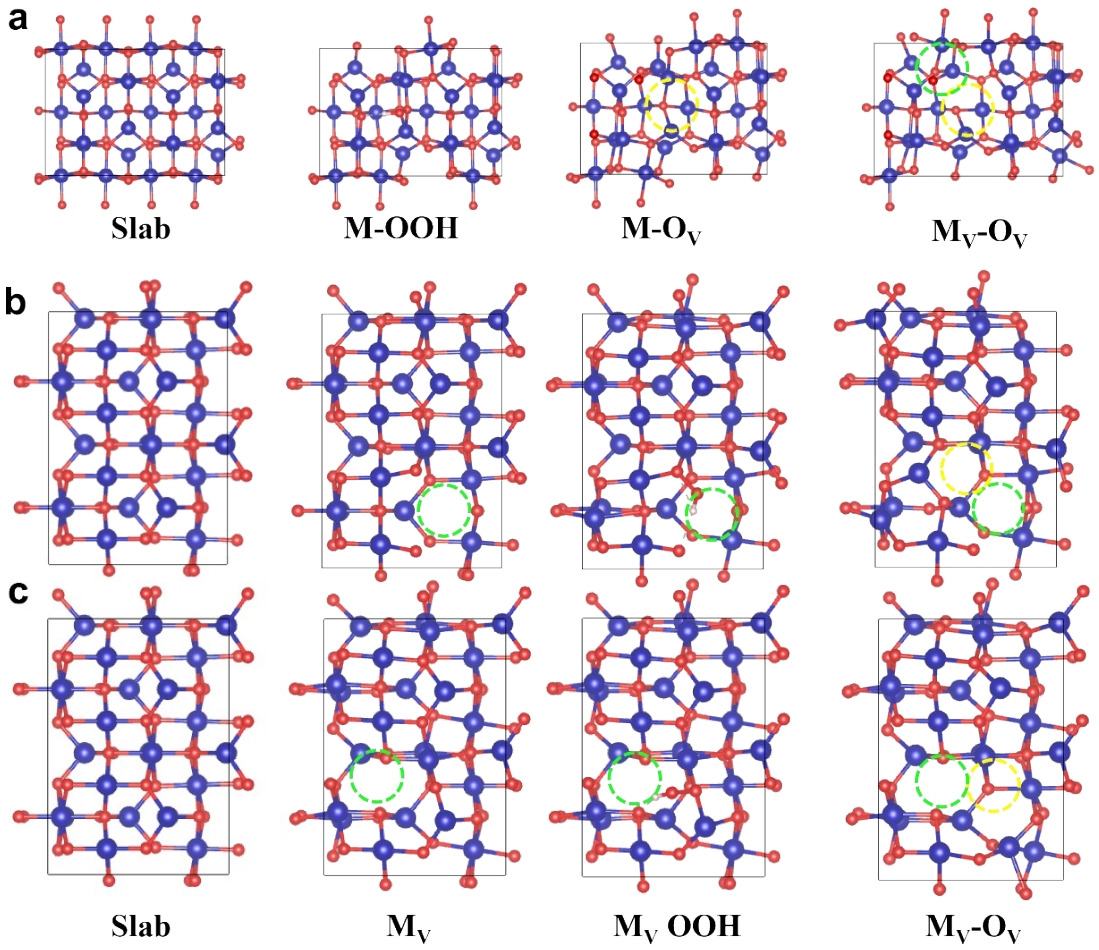

Figure S13. Top view of the model of Co_3O_4 {110} crystal plane in the deactivation process. **a)** O-path. **b)** M-path of Co3. **c)** M-path of Co4. The red sphere is an oxygen atom, the blue sphere is a cobalt atom, and the white sphere is a hydrogen atom. The yellow dashed circles correspond to oxygen vacancies and the green corresponds to metal vacancies.

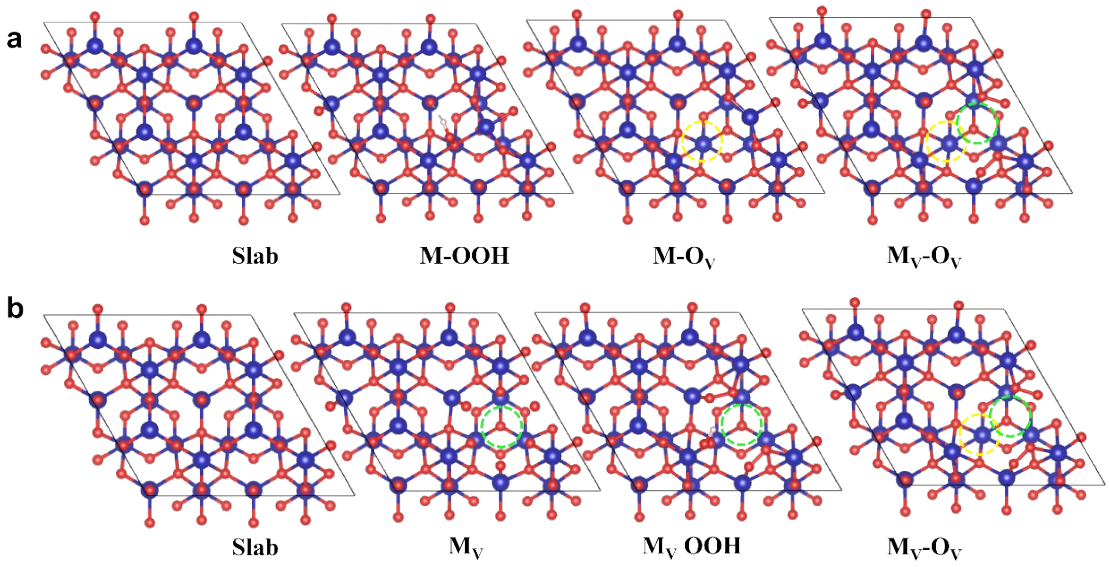

Figure S14. Top view of the model of Co_3O_4 {111} crystal plane in the deactivation process. **a)** O-path. **b)** M-path of Co4. The red sphere is an oxygen atom, the blue sphere is a cobalt atom, and the white sphere is a hydrogen atom. The yellow dashed circles correspond to oxygen vacancies and the green corresponds to metal vacancies.

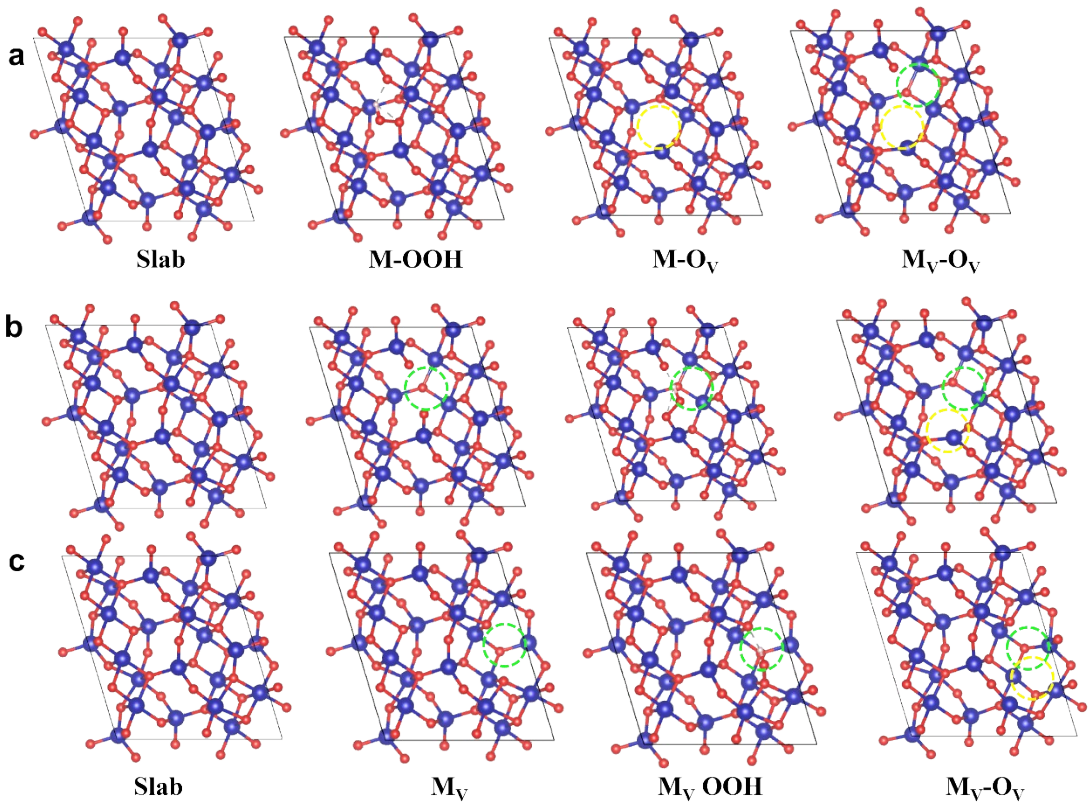

Figure S15. Top view of the model of Co_3O_4 {311} crystal plane in the deactivation process. **a)** O-path. **b)** M-path of Co4. **c)** M-path of Co3. The red sphere is an oxygen atom, the blue sphere is a cobalt atom, and the white sphere is a hydrogen atom. The yellow dashed circles correspond to oxygen vacancies and the green corresponds to metal vacancies.

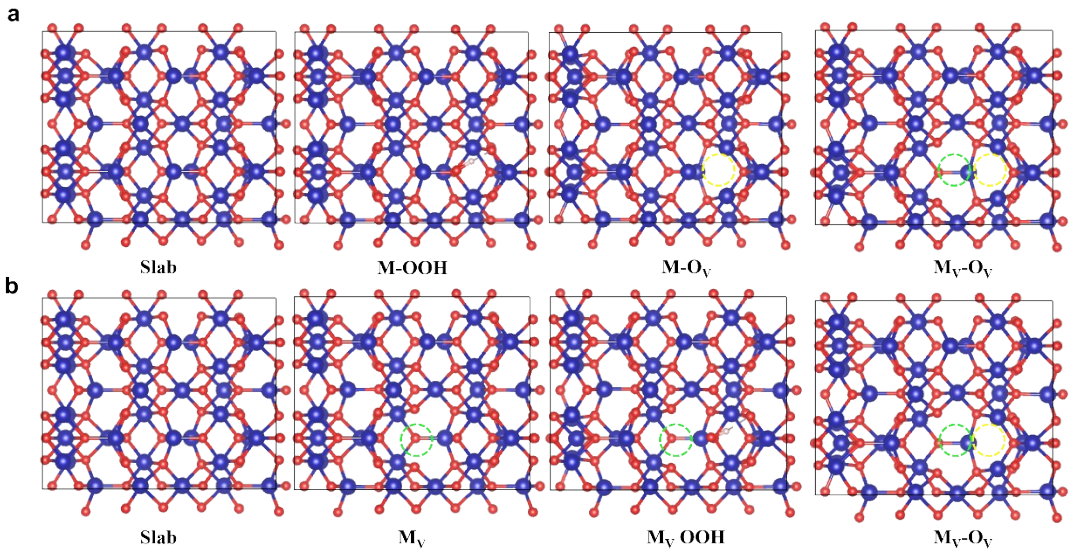

Figure S16. Top view of the model of Co_3O_4 {211} crystal plane in the deactivation process. **a)** O-path. **b)** M-path of Co3. The red sphere is an oxygen atom, the blue sphere is a cobalt atom, and the white sphere is a hydrogen atom. The yellow dashed circles correspond to oxygen vacancies and the green corresponds to metal vacancies.

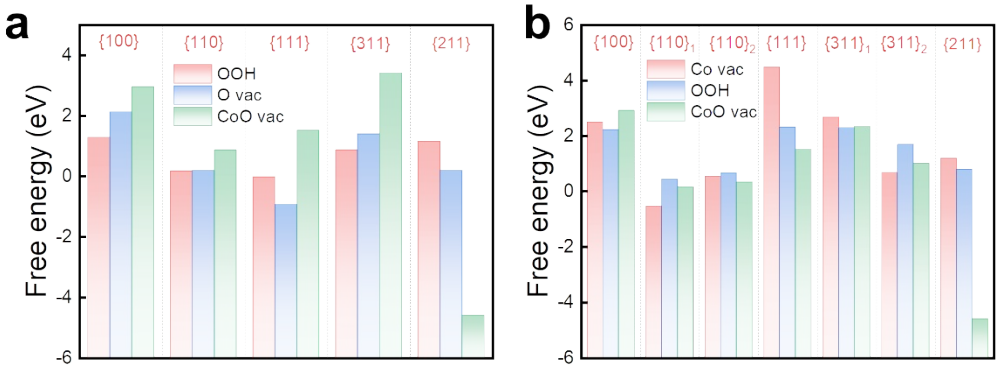

Figure S17. Free energies of elementary steps in dissolution reaction. **a)** O-path. **b)** M-path. See the reaction equations and energies of each path in Table S8-S9.

Table S1. Fitting parameters of the XPS of Co_3O_4 at different times.

Time	Integrated areas				Co^{3+}: Co^{2+}
	Co $2p_{3/2}$				
	Co^{3+}		Co^{3+}	Co^{2+}	
0 h	35253.6	0.23:1	14101.4	60538.8	0.23:1
1 h	8947.9	0.44:1	3579.2	7158.3	0.44:1
4 h	9170.4	0.30:1	4905.9	13330.1	0.30:1
9 h	3795.2	0.28:1	2119.0	6193.4	0.28:1

Table S2 Activity and stability of Cobalt-based catalysts for acidic OER in literature.

Catalysis materials	Preparation methods	Electrolytes	η(mV)@10 mA cm^{-2}	Tafel slope (mV dec^{-1})	Stability-testing periods (h)	Ref
Co_3O_4	Electrodeposition+ calcination	0.5 M H_2SO_4	393	52	12@10 mA cm^{-2}	This work
Co_3O_4	Electron-beam evaporation	0.5 M H_2SO_4	570	80	12@10 mA cm^{-2}	7
Co_3O_4@C/GPO	Calcination	1 M H_2SO_4	360	143	40@10 mA cm^{-2}	8
Co_3O_4/CP	Electrodeposition+ calcination	0.5 M H_2SO_4	420	112	1.5@10 mA cm^{-2}	9
Co_3O_4@C	Electrodeposition+ calcination	0.5 M H_2SO_4	370	82	90@10 mA cm^{-2}	9
Co_3O_4/CeO_2/CP	Electrodeposition+ calcination	0.5 M H_2SO_4	347	88.1	50@10 mA cm^{-2}	3
Co_2TiO_4	Coprecipitated+ calcination	0.5 M H_2SO_4	513	240	10 @1.79 V vs.RHE	10
Ag doped Co_3O_4	Hydrothermal+ calcination	0.5 M H_2SO_4	680	219	10@ 1.8 V vs.RHE	11
Ag doped Co_3O_4	Hydrothermal+ calcination	0.5 M H_2SO_4	470	92	2000 CV cycles between 1.66 and 1.76 V vs. RHE	12
Ba[Co-POM]	Metathesis	1 M H_2SO_4	360	97	24@η=250 mV	13
Mn-doped FeP/$Co_3(PO_4)_2$	Hydrothermal+ Phosphorization	0.5 M H_2SO_4	460	472	>30 000 s@10 mA cm^{-2}	14
$NiCo_2O_4$	Electrodeposition+ calcination	0.5 M H_2SO_4	610	144	10@10 mA cm^{-2}	15

Table S3. Fitting parameters of the reduction peaks of Co_3O_4 at different times (pH=0).

	Peak C1			Peak C2			Peak C3		
Time	xc	A	w	xc	A	w	xc	A	w
(h)	(V vs.RHE)	(V mA)	(V)	(V vs.RHE)	(V mA)	(V)	(V vs.RHE)	(V mA)	(V)
0	1.455	0.025	0.129	1.568	0.003	0.021	1.580	0.005	0.015
0.5	1.468	0.004	0.089	1.542	0.005	0.030	1.575	0.016	0.030
1	1.468	0.005	0.103	1.547	0.008	0.030	1.579	0.022	0.030
2				1.550	0.012	0.032	1.583	0.027	0.032
3				1.554	0.018	0.032	1.587	0.033	0.032
4				1.553	0.021	0.034	1.586	0.032	0.032
5				1.553	0.021	0.034	1.586	0.032	0.032
6				1.549	0.024	0.050	1.584	0.033	0.040
7				1.522	0.017	0.060	1.575	0.043	0.050
8				1.485	0.018	0.080	1.568	0.046	0.060
9				1.468	0.017	0.100	1.559	0.042	0.080
10				1.457	0.012	0.100	1.552	0.029	0.080
11				1.470	0.005	0.100	1.544	0.013	0.080

‘xc’, ‘A’ and ’w’ refers to the peak position area and width of a typical Gaussian peak.

Table S4. Fitting parameters of the reduction peaks of Co_3O_4 at different times (pH=1.4).

	Peak C1			Peak C2			Peak C3		
Time	xc	A	w	xc	A	w	xc	A	w
(h)	(V vs.RHE)	(V mA)	(V)	(V vs.RHE)	(V mA)	(V)	(V vs.RHE)	(V mA)	(V)
0	1.407	0.011	0.125	1.529	0.015	0.036	1.553	0.017	0.022
0.5	1.429	0.009	0.105	1.509	0.008	0.030	1.538	0.012	0.030
1	1.412	0.008	0.110	1.504	0.007	0.030	1.538	0.015	0.030
2	1.410	0.010	0.137	1.512	0.010	0.030	1.543	0.016	0.030
3				1.511	0.012	0.032	1.545	0.019	0.032
4				1.511	0.016	0.034	1.546	0.021	0.032
5				1.509	0.018	0.034	1.544	0.022	0.032
6				1.508	0.020	0.036	1.544	0.022	0.034
7				1.504	0.021	0.038	1.543	0.024	0.036
8				1.503	0.021	0.040	1.543	0.022	0.038
9				1.500	0.020	0.040	1.541	0.021	0.038
10				1.496	0.020	0.045	1.540	0.019	0.040
11				1.487	0.016	0.050	1.536	0.018	0.045
12				1.479	0.010	0.050	1.530	0.013	0.045

'xc', 'A' and 'w' refers to the peak position area and width of a typical Gaussian peak.

Table S5. Fitting parameters of the reduction peaks of Co_3O_4 at different times (pH=2.8).

	Peak C1			Peak C2			Peak C3		
Time	xc	A	w	xc	A	w	xc	A	w
(h)	(V vs.RHE)	(V mA)	(V)	(V vs.RHE)	(V mA)	(V)	(V vs.RHE)	(V mA)	(V)
0	1.380	0.014	0.125	1.477	0.010	0.036	1.509	0.011	0.022
0.5	1.381	0.015	0.105	1.457	0.010	0.030	1.497	0.017	0.030
1	1.381	0.007	0.110	1.452	0.008	0.030	1.492	0.014	0.030
2	1.391	0.007	0.137	1.454	0.009	0.030	1.492	0.015	0.030
3	1.403	0.009		1.460	0.011	0.032	1.496	0.016	0.032
4	1.402	0.007		1.459	0.012	0.034	1.497	0.017	0.032
5	1.402	0.008		1.461	0.013	0.034	1.498	0.019	0.032
6	1.402	0.005		1.461	0.015	0.036	1.499	0.019	0.034
7	1.402	0.006		1.462	0.016	0.038	1.500	0.019	0.036
8	1.402	0.006		1.462	0.017	0.040	1.501	0.021	0.038
9	1.402	0.006		1.464	0.017	0.040	1.503	0.021	0.038
10	1.402	0.005		1.462	0.018	0.045	1.501	0.021	0.040
11				1.448	0.017	0.050	1.495	0.028	0.045
12				1.450	0.018	0.050	1.495	0.027	0.045

'xc', 'A' and 'w' refers to the peak position area and width of a typical Gaussian peak.

Table S6. EIS fitting parameters of Co_3O_4.

Time	RΩ	Cdl	Rp	CΦ	Rs	Rfilm	Cfilm
h	ohm	mF cm^{-2}	ohm	mF cm^{-2}	ohm	ohm	mF cm^{-2}
0	1.462	0.0041	0.0213	0.184	51.24	0.0300	0.1144
1	1.499	0.0037	0.0594	0.1792	94.11	0.1329	0.4926
4	1.583	0.0018	0.3066	0.1601	1736	0.8089	0.3138
5	1.619	0.0029	0.5533	0.1414	2266	1.357	0.2
9	1.66	0.0078	0.593	0.06258	2911	5.842	0.05497

Table S7. The reaction formula of the two dissolving paths of Co_3O_4 used for energy calculation.

O-path	
Step1	$*+H_2O+0e^- \rightarrow *Ovac-OOH+0.5H_2+e^-$
Step2	$*Ovac-OOH+0.5H_2+e^- \rightarrow *Ovac+H_2+O_2+2e^-$
Step3	$*Ovac+H_2+O_2+2e^- \rightarrow *Ovac-Covac+Co^{2+}+H_2+O_2+4e^-$
M-path	
Step1	$*+H_2O+0e^- \rightarrow *Covac+Co^{2+}+H_2O+2e^-$
Step2	$*Covac+Co^{2+}+H_2O+2e^- \rightarrow *Covac-Ovac-OOH+Co^{2+}+0.5H_2+3e^-$
Step3	$*Covac-Ovac-OOH+Co^{2+}+0.5H_2+2e^- \rightarrow *Covac-Ovac++Co^{2+}+H_2+O_2+4e^-$

Table S8. Free energy (eV) of intermediates on different crystal planes of Co_3O_4 following O-path.

	slab	OOH	O vac	CoO vac
{100}	0	1.29194	2.12773	2.96253
{110}	0	0.17401	0.18953	0.86872
{111}	0	-0.01761	-0.92366	1.52066
{311}	0	0.86743	1.40186	3.42149
{211}	0	1.15898	0.19164	-4.58905

Table S9. Free energy (eV) of intermediates on different crystal planes of Co_3O_4 following M-path.

	slab	Co vac	OOH	CoO vac
{100}	0	2.49692	2.22673	2.9201
{110}	0	-0.52461	0.44406	0.16442
{110}	0	0.54807	0.67216	0.3408
{111}	0	4.49283	2.31996	1.52066
{311}	0	2.67612	2.29769	2.34123
{311}	0	0.68508	1.70088	1.01558
{211}	0	1.20229	0.79418	-4.58905

Reference

1 L. G. Bloor, P. I. Molina, M. D. Symes and L. Cronin, Low pH Electrolytic Water Splitting Using Earth-Abundant Metastable Catalysts That Self-Assemble in Situ, *J. Am. Chem. Soc.*, 2014, **136**, 3304–3311.

2 X.-H. Xia, J.-P. Tu, X.-L. Wang, C.-D. Gu and X.-B. Zhao, Mesoporous Co3O4 monolayer hollow-sphere array as electrochemical pseudocapacitor material, *Chem. Commun.*, 2011, **47**, 5786–5788.

3 J. Huang, H. Sheng, R. D. Ross, J. Han, X. Wang, B. Song and S. Jin, Modifying redox properties and local bonding of Co3O4 by CeO2 enhances oxygen evolution catalysis in acid, *Nat. Commun.*, 2021, **12**, 3036.

4 R. L. Doyle, I. J. Godwin, M. P. Brandon and M. E. G. Lyons, Redox and electrochemical water splitting catalytic properties of hydrated metal oxide modified electrodes, *Phys Chem Chem Phys*, 2013, **15**, 13737–13783.

5 M. E. G. Lyons and M. P. Brandon, The significance of electrochemical impedance spectra recorded during active oxygen evolution for oxide covered Ni, Co and Fe electrodes in alkaline solution, *J. Electroanal. Chem.*, 2009, **631**, 62–70.

6 E. M. Garcia, J. S. Santos, E. C. Pereira and M. B. J. G. Freitas, Electrodeposition of cobalt from spent Li-ion battery cathodes by the electrochemistry quartz crystal microbalance technique, *J. Power Sources*, 2008, **185**, 549–553.

7 J. S. Mondschein, J. F. Callejas, C. G. Read, J. Y. C. Chen, C. F. Holder, C. K. Badding and R. E. Schaak, Crystalline Cobalt Oxide Films for Sustained Electrocatalytic Oxygen Evolution under Strongly Acidic Conditions, *Chem. Mater.*, 2017, **29**, 950–957.

8 J. Yu, F. A. Garcés-Pineda, J. González-Cobos, M. Peña-Díaz, C. Rogero, S. Giménez, M. C. Spadaro, J. Arbiol, S. Barja and J. R. Galán-Mascarós, Sustainable oxygen evolution electrocatalysis in aqueous 1 M H2SO4 with earth abundant nanostructured Co3O4, *Nat. Commun.*, 2022, **13**, 4341.

9 Xiulin Yang, Henan Li, Ang-Yu Lu, Shixiong Min, Zacharie Idriss, Zacharie Idriss, Mohamed N. Hedhili, Kuo-Wei Huang, Hicham Idriss, and Lain-Jong Li, Highly acid-durable carbon coated Co3O4 nanoarrays as efficient oxygen evolution electrocatalysts, *Nano Energy*, 2016, **25**, 42–50.

10 S. Anantharaj, K. Karthick and S. Kundu, Spinel Cobalt Titanium Binary Oxide as an All-Non-Precious Water Oxidation Electrocatalyst in Acid, *Inorg. Chem.*, 2019, **58**, 8570–8576.

11 Kai-Li Yan, Jing-Qi Chi, Jing-Yi Xie, Bin Dong, Zi-Zhang Liu, Wen-Kun Gao, Jia-Hui Lin, Yong-Ming Chai, and Chenguang Liu, Mesoporous Ag-doped Co3O4 nanowire arrays supported on FTO as efficient electrocatalysts for oxygen evolution reaction in acidic media, *Renew. Energy*, 2018, **119**, 54–61.

12 Kai-Li Yan, Jun-Feng Qin, Jia-Hui Lin, Bin Dong, Jing-Qi Chi, Zi-Zhang Liu, Fangna Dai, Yong-Ming Chai, and Chenguang Liu, Probing the active sites of Co3O4 for the acidic oxygen evolution reaction by modulating the

Co2+/Co3+ ratio, *J. Mater. Chem.*, 2018, **6**, 5678–5686.
13 M. Blasco-Ahicart, J. Soriano-Lopez, J. J. Carbo, J. M. Poblet and J. R. Galan-Mascaros, Polyoxometalate electrocatalysts based on earth-abundant metals for efficient water oxidation in acidic media, *Nat. Chem.*, 2018, **10**, 24–30.
14 H. Liu, X. Peng, X. Liu, G. Qi and J. Luo, Porous Mn-Doped FeP/Co3(PO4)2 Nanosheets as Efficient Electrocatalysts for Overall Water Splitting in a Wide pH Range, *ChemSusChem*, 2019, **12**, 1334–1341.
15 J. Yin, J. Jin, M. Lu, B. Huang, H. Zhang, Y. Peng, P. Xi and C.-H. Yan, Iridium Single Atoms Coupling with Oxygen Vacancies Boosts Oxygen Evolution Reaction in Acid Media, *J. Am. Chem. Soc.*, 2020, **142**, 18378–18386.